

Anharmonic inter-layer bonding leads to intrinsically low thermal conductivity of bismuth oxychalcogenides

Hong-Yue Song, Xu-Jin Ge, Man-Yu Shang, and Jing-Tao Lü

School of Physics and Wuhan National High Magnetic Field Center,

Huazhong University of Science and Technology, 430074 Wuhan, P. R. China

Abstract

The anharmonicity of phonons in solid is ultimately rooted in the chemical bonding. However, the direct connection between phonon anharmonicity and chemical bonding is difficult to make experimentally or theoretically, due mainly to their complicated lattice structures. Here, with the help of density functional theory based calculations, we discovery that electrostatic inter-layer coupling in $\text{Bi}_2\text{O}_2\text{X}$ ($\text{X}=\text{S},\text{Se},\text{Te}$) leads to intrinsically low lattice thermal conductivity. We explain our discovery by the strong anharmonic chemical bonding between Bi and chalcogen atoms. Our results shed light on the connection between inter-layer chemical bonding and phonon anharmonicity, which could be explored in a wide range of layered materials.

I. INTRODUCTION

Materials with low thermal conductivity may find applications in many disciplines including thermoelectrics^{1,2}, heat insulation and phononic devices³. Phonons are main heat carriers in semiconductors and insulators. Phonon engineering of thermal conductivity has witnessed tremendous progress in recent years⁴⁻⁶. Different extrinsic and intrinsic approaches have been developed to reduce the phonon thermal conductivity (κ). Among them are nanostructuring, defect engineering, and enhancing phonon anharmonicity. Anharmonic phonon scattering is an intrinsic mechanism that leads to finite κ ^{1,7-9}. Thus, utilizing strong phonon anharmonicity is an attractive way to reduce κ , while keeping other properties intact¹⁰. Generally, weak chemical bonds lead to large anharmonicity due to large atomic displacement involved. As a rule of thumb, complicate lattice structure with heavy elements is believed to lead to strong anharmonicity. But their microscopic mechanism is difficult to pinpoint.

Layered materials have weak inter-layer bonding and many show low κ and good thermoelectric performance¹¹. They normally have good electrical transport property in the plane and low κ across the plane. For thermoelectric applications, it is highly desirable to reduce the in-plane κ (κ_{\parallel}) through phonon engineering. As a kind of thermoelectric material, layered bismuth oxychalcogenides $\text{Bi}_2\text{O}_2\text{X}$ ($\text{X}=\text{S}, \text{Se}, \text{Te}$) (BOX) have been studied experimentally¹²⁻¹⁶. But their thermoelectric performance is mainly hindered by the poor electrical transport property. Very recently, thin layer of single crystal layered oxychalcogenide, $\text{Bi}_2\text{O}_2\text{Se}$, has been successfully synthesized^{17,18}. Its high electron mobility, strong spin-orbit interaction and ultrafast infrared response lead to potential applications in nano-electronics, opto-electronics, topological devices and ferroelectricity¹⁹⁻²¹. The electronic band structure of $\text{Bi}_2\text{O}_2\text{Se}$ has been mapped out combining angle-resolved photoemission spectroscopy and density functional theory (DFT) calculations²². The experimental progress makes it possible to enhance the thermoelectric performance by, i.e., tuning of carrier concentration²³.

Despite the above mentioned progress in characterizing the electric properties, the phonon transport properties of BOX are still poorly understood, which hinders the in-depth understanding in its electronic, optoelectronic and thermal properties. Here, using DFT based calculations, we show that, BOX has low intrinsic in-plane κ (κ_{\parallel}). This means high electrical conductivity and low phonon thermal conductivity can in principle be realised simultane-

ously in the same direction. Based on the analysis of its phonon spectrum, scattering lifetime, Grüneisen parameters and real-space electron distribution, we are able to show unambiguously that, the low κ_{\parallel} originates from strong anharmonic inter-layer bonding between Bi and chalcogen atoms. Our results shed light on the connection between chemical bonding and phonon anharmonicity, and showed that inter-layer coupling can be used to tune κ_{\parallel} in layered materials.

II. RESULTS AND DISCUSSIONS

A. Structure and phonon dispersion

Bulk $\text{Bi}_2\text{O}_2\text{Se}$ and $\text{Bi}_2\text{O}_2\text{Te}$ crystallize in the $(\text{Na}_{0.25}\text{Bi}_{0.75})_2\text{O}_2\text{Cl}$ type structure, and belong to tetragonal space group $I4/mmm$ (139) with 10 atoms in one unit cell as shown in Figure 1 (b). Meanwhile, $\text{Bi}_2\text{O}_2\text{S}$ has a distorted structure, where the Bi atoms slide slightly apart, and belongs to the $Pnmm$ (58) group with lower symmetry (Figure 1 (a)). This structure distortion changes the chemical bonding environment of S and brings a small anisotropy between x and y direction. We will show below that it has important effect on κ . There are two electron transfer from the Bi_2O_2 layer to chalcogen layer, and the two layers are bonded through electrostatic force. The optimized lattice parameters, the dielectric constant and Born effective charge of each atom are listed in Table 1 and 2 of the Supporting Information (SI). We have also calculated the electronic band structures from the optimized lattice parameters. They show good agreement with previous works (SI, Figure 1).

Figure 1 (d-f) show the atomically resolved phonon dispersion and the corresponding density of states (DOS) projected onto different atoms. We observe a phonon gap at ~ 6 THz, separating the spectrum, albeit small in $\text{Bi}_2\text{O}_2\text{S}$. The high frequency part of the spectrum is contributed dominantly by O atoms. The corresponding dispersion and DOS are very similar for all three materials. Although O and Bi atoms are strongly bonded in the same layer, their motions are decoupled due to large mass mis-match. On the other hand, although Bi and chalcogen atoms are at different layers, they couple together and form the low frequency phonon band. This clear separation of O vibration from others makes our analysis easier.

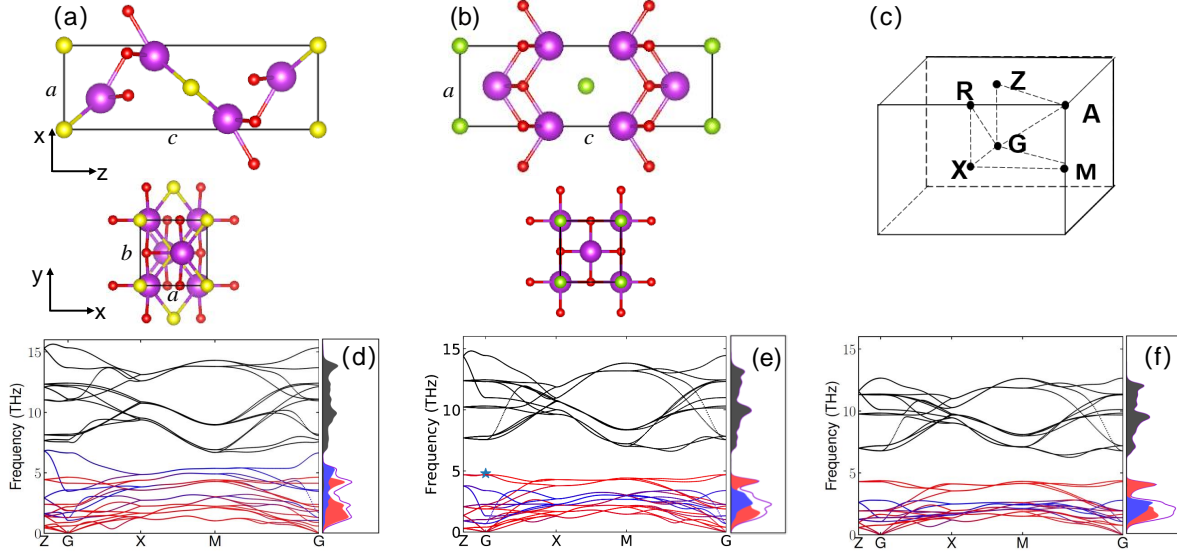


FIG. 1: (a-b) Side and top view of the atomic structure of $\text{Bi}_2\text{O}_2\text{X}$ (X=S, Se, Te). The Se and Te atom locates between two Bi_2O_2 layers, and has 8 nearest neighbouring Bi atoms, 4 from each layer (b). $\text{Bi}_2\text{O}_2\text{S}$ has a lower symmetry with slightly distorted structure, with 4 nearest neighbours, 2 from each layer (a). (c) The high symmetry points in the first Brillouin zone: Γ (0.0, 0.0, 0.0), X (0.5, 0.0, 0.0), M (0.5, 0.5, 0.0), A (0.5, 0.5, 0.5), R (0.5, 0.0, 0.5), Z (0.0, 0.0, 0.5). (d-f) The atomically-resolved phonon dispersion and density of states. The red, blue and black colors correspond to projection onto Bi, chalcogene, and O atoms, respectively. The solid line represents the total DOS. The blue star in (e) marks the frequency of the Raman active A_{1g} mode measured experimentally²⁴. The phonon bands can be divided into a low frequency and a high frequency part. They are separated by a band gap. In the low frequency part, Bi (red) and chalcogen (blue) atom couple together. The high frequency part is contributed almost entirely by O atoms (black).

B. Thermal conductivity

We calculate κ using the Boltzmann transport equation (BTE) within the single mode relaxation time approximation (RTA) as implemented in Phonopy²⁵ and Phono3py²⁶ package. The results are shown in Figure 2. More details of the results are shown in Figures 2-4 of SI. Consistent with their layered structure, all materials show anisotropic κ , with $\kappa_{\parallel} > \kappa_z$. $\text{Bi}_2\text{O}_2\text{S}$ and $\text{Bi}_2\text{O}_2\text{Te}$ show similar low $\kappa_{x/y}$, which is below 1 W/m-K at T=300 K, while $\text{Bi}_2\text{O}_2\text{Se}$ has around two-fold larger value. We note that, κ we obtained for BOX is comparable to values of other thermoelectric materials, including SnSe²⁷⁻²⁹, Bi_2Te_3 , PbX (X=S, Se, Te) and BiCuOX (X=S, Se, Te)³⁰⁻³². Due to their similar lattice structure, we

have performed detailed comparison to BiCuOX in the SI (Figures 5-9 and Table 3). Additionally, we notice that $\text{Bi}_2\text{O}_2\text{S}$ shows lower κ than $\text{Bi}_2\text{O}_2\text{Se}$. Normally, from S to Te, we expect κ to decrease with increasing atomic mass for similar lattice structures. We may attribute this abnormal behavior of $\text{Bi}_2\text{O}_2\text{S}$ to its structure distortion. The purpose of the rest analysis is to give a microscopic explanation of the above mentioned features in κ .

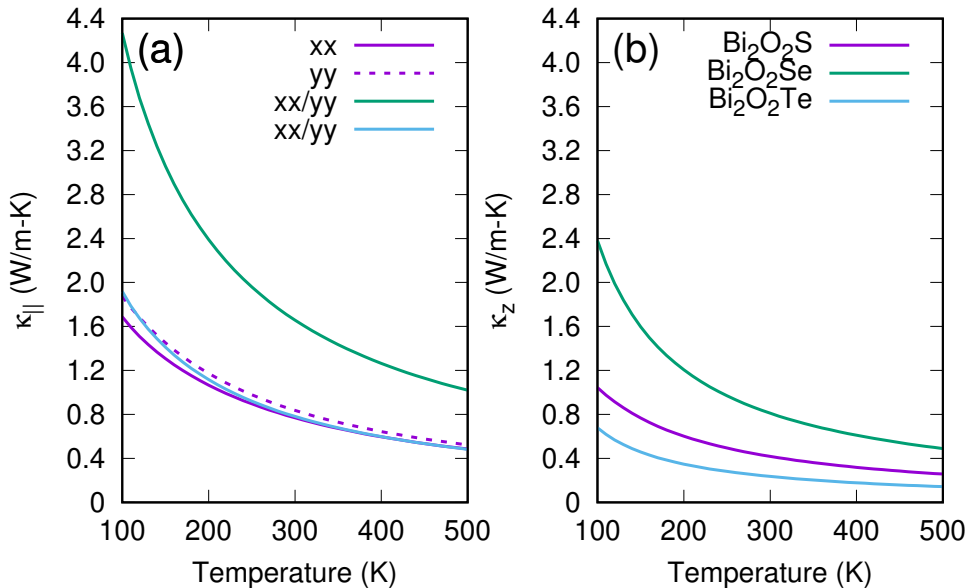


FIG. 2: The in-plane (a) and out-of-plane (b) phonon thermal conductivity as a function of temperature. The layered structure in $\text{Bi}_2\text{O}_2\text{X}$ leads to anisotropy in κ , i.e., $\kappa_{||} > \kappa_z$.

As shown in Eq. (2) of Methods, within all the parameters that κ depends, the relaxation time τ_λ is determined by anharmonic phonon scattering, while all the rest terms are determined by the harmonic phonon spectrum. To find the origin of low κ in $\text{Bi}_2\text{O}_2\text{X}$, firstly we set $\tau_\lambda = 1$, and show the accumulative sum of frequency dependent $\kappa(\omega)$ (Eq. 3 of Methods) in Figure 3 (a). $\text{Bi}_2\text{O}_2\text{S}$ shows the largest value, opposite to the results of κ . This means lower κ of $\text{Bi}_2\text{O}_2\text{S}$ does not come from the harmonic phonon spectrum, but from their shorter τ_λ . We have also shown a comparison to BiCuOX (X=S, Se, Te) in Figure 7 of the SI. We find that, although they have similar κ , the band structure contribution to κ in BOX is much larger than BiCuOX. This suggests stronger anharmonic scattering and hence smaller τ_λ in BOX, which we focus on in the following.

C. Anharmonic scattering

Figure 4 shows the distribution of scattering lifetime τ as a function of frequency for the three materials considered. The high frequency part shows little frequency dependence and is of similar magnitude for all materials. The low frequency part has a much wider distribution. But it is still clear that, the data of $\text{Bi}_2\text{O}_2\text{Se}$ locate in higher τ region compared to $\text{Bi}_2\text{O}_2\text{Te}$ and $\text{Bi}_2\text{O}_2\text{S}$. This confirms the expectation that, lower κ of $\text{Bi}_2\text{O}_2\text{S}$ and $\text{Bi}_2\text{O}_2\text{Te}$ originates from its shorter τ and hence stronger anharmonic scattering. Considering their similar lattice structure, shorter τ of $\text{Bi}_2\text{O}_2\text{Te}$ compared to $\text{Bi}_2\text{O}_2\text{Se}$ can be understood due to larger mass of Te. However, this can not explain why $\text{Bi}_2\text{O}_2\text{S}$ shows the lowest τ distribution in the low frequency regime. Thus, we need further analysis of τ .

The magnitude of τ depends both on the scattering phase space and on the strength of anharmonic potential. We can separate the two contributions. Figure 3(b) compares the joint DOS (JDOS) of 3-phonon scattering in all materials. We find that with increasing atomic number from S, Se to Te, JDOS in the low frequency regime grows up. The reason is that, heavier mass leads to narrower phonon spectrum and stronger overlap between different modes. This tends to increase the phase space for anharmonic phonon scattering. Although the change of JDOS may partly explain different κ of $\text{Bi}_2\text{O}_2\text{Se}$ and $\text{Bi}_2\text{O}_2\text{Te}$, it still can not explain the lower κ of $\text{Bi}_2\text{O}_2\text{S}$.

We now turn to the anharmonic potential, the strength of which can be characterized by the Grüneisen parameters (γ). To further correlate with the atomic chemical bonding, in Table IV, we show the projected γ on different atoms in three directions. As a common feature, we get larger γ for Bi and chalcogen atoms compared to O atoms. These results suggest that inter-layer Bi-X bonding in BOX is strongly anharmonic and generates stronger phonon scattering. This is the common feature of all three kinds of materials. The low κ of $\text{Bi}_2\text{O}_2\text{S}$ can also be understood from the Grüneisen parameter. The lattice distortion in $\text{Bi}_2\text{O}_2\text{S}$ makes the x and y direction anisotropic. This is reflected in the Grüneisen parameters. γ of S in y direction is reduced, while that in x and z gets much larger, promoting the inter-layer anharmonicity. This information suggests that, we can attribute the smaller scattering lifetime and lower κ of $\text{Bi}_2\text{O}_2\text{S}$ to the enhancement of anharmonic inter-layer coupling generated by lattice distortion.

Further comparison to BiCuOX supports our above arguments. In BiCuOX, chalcogen

atom and Cu form stronger bonds. This reduces the anharmonic inter-layer coupling between BiO and CuX layers. This is reflected in the projected Grüneisen parameters. First, in BiCuOX, γ in z direction is consistently smaller than that of in-plane (x/y) direction for all atoms. Second, Cu atoms show the largest γ instead of chalcogen atoms in BOX. The reduction of γ , together with their smaller JDOS (SI, Figure 8), leads to much longer scattering lifetime (SI, Figure 9).

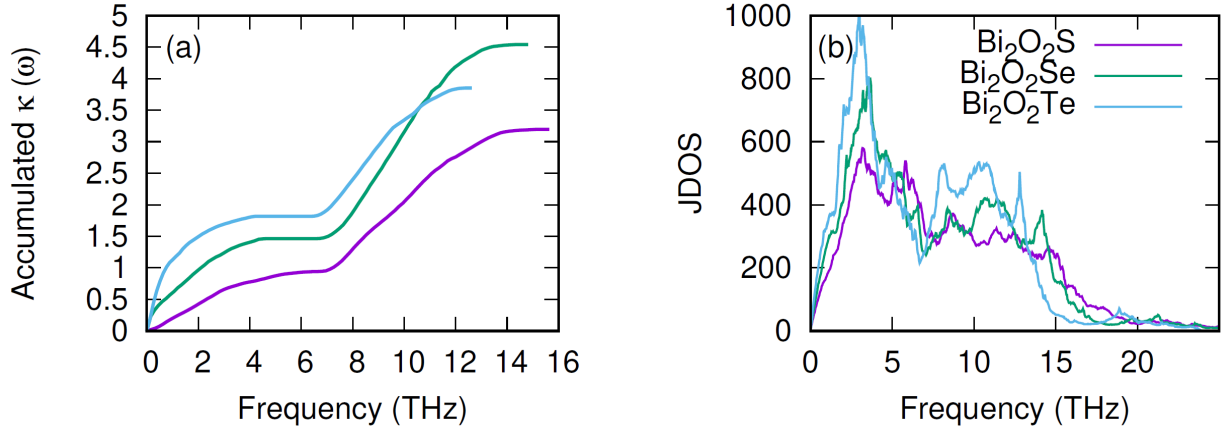


FIG. 3: (a) The relative magnitude of phonon band structure contribution to the accumulated phonon thermal conductivity. (b) The joint density of states (JDOS) for 3-phonon scattering as a function of frequency.

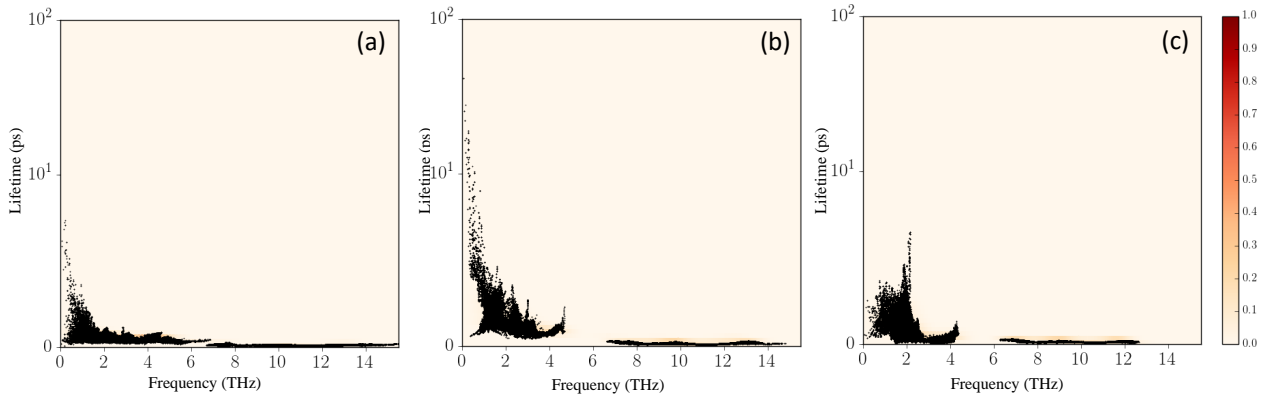


FIG. 4: Distribution of relaxation time as a function of frequency for (a) Bi₂O₂S, (b) Bi₂O₂Se, (c) Bi₂O₂Te, respectively.

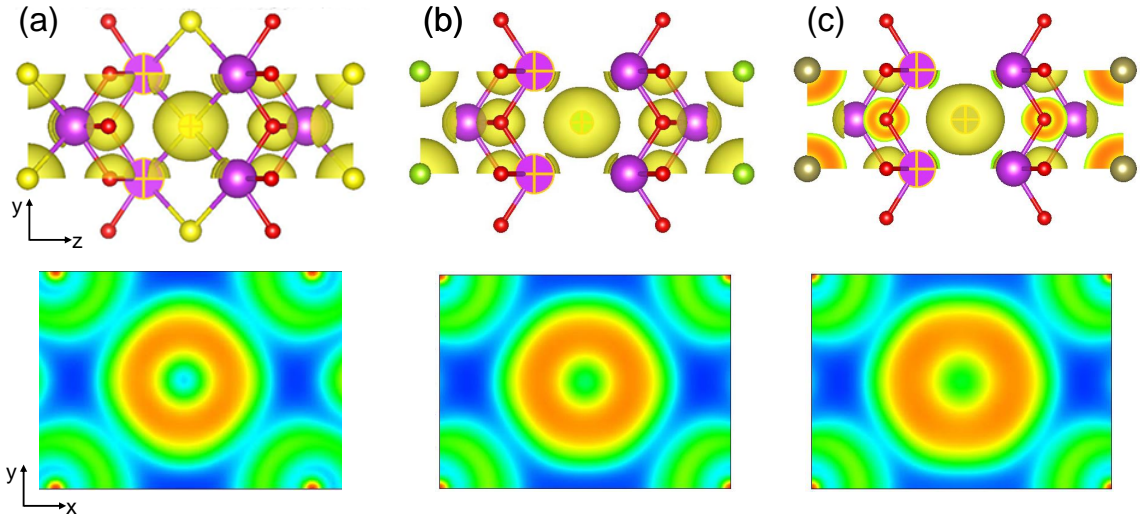


FIG. 5: Electron localization function (ELF) of (a) Bi₂O₂S, (b) Bi₂O₂Se and (c) Bi₂O₂Te. The upper panel shows the atomic structure and the isosurfaces at 0.6. The LPE of Bi is seen as caps near Bi atoms. The lower panel shows the plane cut defined by the three atoms marked by crosses. The ELF is plotted from 0 (blue) to 1 (red). Comparing the distribution in the lower panels, we can see that the ELF distribution spreads further out, which means that the lattice distortion enhances the inter-layer coupling between S and Bi.

material	γ	Bi(x)	Bi(y)	Bi(z)	X(x)	X(y)	X(z)	O(x)	O(y)	O(z)
		Bi ₂ O ₂ S	4.79	4.79	4.02	4.70	2.40	4.93	1.30	1.43
Bi ₂ O ₂ Se	4.27	4.27	3.42	4.05	4.05	4.34	1.96	1.96	1.93	
Bi ₂ O ₂ Te	3.60	3.60	3.07	3.76	3.76	5.20	1.71	1.71	1.50	

TABLE I: Projected Grüneisen parameters γ on different atoms and directions in Bi₂O₂X.

D. Origin of the strong anharmonicity

From the above analysis, we can attribute low κ of BOX to large anharmonic coupling between Bi and chalcogen atoms. The lattice distortion of Bi₂O₂S further enhances the anharmonicity. The next question we ask is what is the microscopic mechanism of the strong anharmonicity. We will now make connection to its atomic structure and chemical bonding. In BOX, each chalcogen atom is surrounded by a Bi cage with eight Bi atoms. Due to the inter-layer charge transfer, the chalcogen atom interacts mainly through electrostatic force with surrounding Bi atoms, forming weak ionic bonds. Their bonding environment

can be characterized through the electron localization function (ELF)³³ (Figure 5), which shows clear ionic bonding between atoms. The small caps near Bi represents its lone-pair electrons (LPE), which also contribute to the inter-layer coupling, i.e., they interact through electrostatic force with the chalcogen atoms. As for Bi₂O₂S, after lattice distortion, four Bi atoms move even closer S. This further enhances their mutual interaction, which can be seen from the plane cut in the lower panel of Figure 5 (a). Comparing to (b) and (c), the strongest bonding between S and Bi can be deduced. This is the microscopic reason why Bi₂O₂S has κ as low as Bi₂O₂Te and much lower than Bi₂O₂Se.

III. CONCLUSIONS

To conclude, we have predicted low phonon thermal conductivity of bismuth oxychalcogenides Bi₂O₂X (X=S, Se, Te). Through careful analysis of their phonon properties, we can ultimately correlate the strong anharmonicity and hence low thermal conductivity to the inter-layer bonding between Bi and chalcogen atoms. The strong correlation between bond anharmonicity and low thermal conductivity gives atomic insights of the thermal properties of materials. The same principle can be applied to a broad range of layered materials with electrostatic inter-layer coupling.

IV. METHODS

A. DFT calculations

For the first-principles calculations, we use density functional theory (DFT) with the projected augmented wave (PAW) method as implemented within the Vienna *ab initio* Simulation Package (VASP)^{34,35}. We choose the Perdew-Bueke-Ernzerhof (PBE)³⁶ version of generalized gradient approximation (GGA) to treat the exchange-correlation interaction. The plane wave cut-off energy is set as 550 eV. The Brillouin zone is sampled by using the Monkhorst-Pack scheme³⁷ with $9 \times 9 \times 3$ mesh k-points to optimize the structure until the forces on the atoms are less than 0.01 eV/Å.

To calculate the phonon dispersion and phonon conductivity, we use phonopy²⁵ and phono3py²⁶ codes together with VASP^{34,35}. The second and third order force constants are calculated by finite-difference method. We use $5 \times 5 \times 2$ supercell for the second order force

constant, and $3 \times 3 \times 2$ supercell for the third order force constant. We have also performed the $4 \times 4 \times 2$ supercell calculation to confirm the convergence of the third order forces. We set the convergence criteria to 10^{-8} eV for self-consistent loop and 0.01 eV/Å for the force. The Γ -only scheme is used to sample the reciprocal cell of the supercell.

B. Thermal conductivity

The linearized phonon BTE with the single mode RTA is used to calculate the phonon thermal conductivity with $21 \times 21 \times 21$ sampling mesh using phono3py²⁶. We first define

$$\vec{\kappa}_\lambda = C_\lambda \vec{v}_\lambda \otimes \vec{v}_\lambda \tau_\lambda, \quad (1)$$

as contribution of each mode λ to the thermal conductivity. Here, C_λ is the heat capacity of mode λ , \vec{v}_λ is the group velocity, and τ_λ is the relaxation time. The frequency-resolve version is then written as

$$\vec{\kappa}(\omega) = \sum_\lambda \delta(\omega - \omega_\lambda) \vec{\kappa}_\lambda. \quad (2)$$

The accumulated sum plotted in Fig. 4 is calculated as

$$\vec{\kappa}_s(\omega) = \sum_{\omega_\lambda \leq \omega} \vec{\kappa}_\lambda, \quad (3)$$

with τ_λ set to 1. Finally, the thermal conductivity κ is expressed as

$$\vec{\kappa} = \frac{1}{V} \sum_\lambda \kappa_\lambda, \quad (4)$$

where V is the volume of the system.

C. The joint density of states

The joint density states can be used to quantify the phase space for phonon anharmonic scattering, determined by the phonon dispersion relation. The results shown in Fig. 4 (b) is

for 3-phonon scattering and calculated from

$$\begin{aligned}
 D(\omega) &= \frac{1}{N} \sum_{\lambda_1, \lambda_2} [\delta(\omega + \omega_{\lambda_1} - \omega_{\lambda_2}) + \delta(\omega - \omega_{\lambda_1} + \omega_{\lambda_2})] \\
 &+ \frac{1}{N} \sum_{\lambda_1, \lambda_2} \delta(\omega - \omega_{\lambda_1} - \omega_{\lambda_2}).
 \end{aligned} \tag{5}$$

D. The projected Grüneisen parameter

The mode-resolved Grüneisen parameters are calculated within the quasi-harmonic approximation using Phonopy. To characterize the anharmonicity of each atom, we define the projected Grüneisen parameter by projecting all the modes to given atom in a given direction as following

$$\gamma_{i\alpha} = \frac{\sum_{\lambda} \gamma_{\lambda} e_{\lambda, i\alpha}}{\sum_{\lambda} e_{\lambda, i\alpha}}. \tag{6}$$

Here, γ_{λ} is the Grüneisen parameter of mode λ , i is the atom index, α represents the direction, and $e_{\lambda, i\alpha}$ is the element of the eigen vector e_{λ} corresponding to atom i in direction α .

ACKNOWLEDGMENTS

The authors are supported by the National Key Research and Development Program of China (Grant No. 2017YFA0403501), the National Natural Science Foundation of China (Grant No. 21873033) and the program for HUST academic frontier youth team. They thank the National Supercomputing Center in Shanghai for providing computational resources.

Appendix A: Electronic structure

Based on the relaxed lattice structure, the electronic band structure is calculated in the modified Becke-Johnson meta-GGA potential^{38,39} including the spin-orbit interaction. The results are shown in Figure 6. We get a band gap of 1.38 eV, 0.91 eV and 0.23 eV for Bi₂O₂S, Bi₂O₂Se and Bi₂O₂Te, respectively. They are comparable to experimental observations. The DOS plots show that at the top of the valence band, the contribution of S/Se/Te atom is dominant, while at the bottom of the conduction band the contribution of Bi atoms is

dominant. Further analysis shows that, for all cases, the contribution mainly comes from the p orbitals.

	a (Å)	b (Å)	c (Å)	$\varepsilon_{x/y}$	ε_z
$\text{Bi}_2\text{O}_2\text{S}$	3.98	3.89	12.08	10.02/11.36	9.42
$\text{Bi}_2\text{O}_2\text{Se}$	3.93	3.93	12.40	13.86/13.86	10.34
$\text{Bi}_2\text{O}_2\text{Te}$	4.02	4.02	12.88	17.21/17.21	12.00

TABLE II: Calculated lattice parameters, static dielectric tensor (ε) of BOX.

	$z_{\text{Bi},x/y}$	$z_{\text{Bi},z}$	$z_{\text{X},x/y}$	$z_{\text{X},z}$	$z_{\text{O},x/y}$	$z_{\text{O},z}$
$\text{Bi}_2\text{O}_2\text{S}$	5.17/5.91	5.17	-3.30/-4.32	-3.26	-3.50/-3.75	-3.54
$\text{Bi}_2\text{O}_2\text{Se}$	6.12/6.12	5.39	-4.33/-4.33	-3.12	-3.96/-3.96	-3.82
$\text{Bi}_2\text{O}_2\text{Te}$	6.54/6.54	5.67	-4.35/-4.35	-3.21	-4.33/-4.33	-4.05

TABLE III: Calculated Born effective charge (z) for ions in the unit of e for BOX.

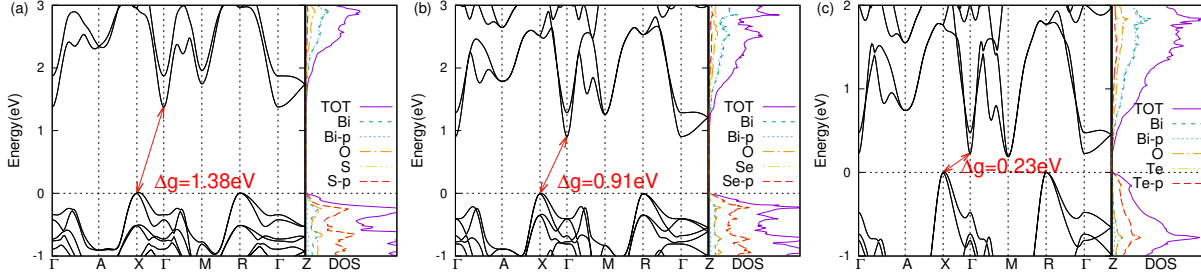


FIG. 6: Band structure, atomic and orbital decomposition of density of states of bulk $\text{Bi}_2\text{O}_2\text{S}$ (a), $\text{Bi}_2\text{O}_2\text{Se}$ (b), $\text{Bi}_2\text{O}_2\text{Te}$ (c).

Appendix B: Phonon properties of $\text{Bi}_2\text{O}_2\text{X}$

Tables II-III give the calculated lattice parameters, the static dielectric constants and the Born effective charges of $\text{Bi}_2\text{O}_2\text{X}$ ($\text{X}=\text{S}, \text{Se}, \text{Te}$) (BOX). Figures 7-9 give the details of the phonon thermal conductivity (κ) calculation.

Appendix C: Comparison to BiCuOX

BiCuOX ($\text{X}=\text{S}, \text{Se}, \text{Te}$) has similar structure to BOX. Figure 10 shows their lattice structure, corresponding phonon spectrum, and projected density of states onto different atoms. κ of BiCuOX is also comparable to BOX. Thus, we here give some comparison

material	γ							
	Bi(x/y)	Bi(z)	X(x/y)	X(z)	O(x/y)	O(z)	Cu(x/y)	Cu(z)
Bi ₂ O ₂ S	4.79/4.79	4.02	4.70/2.40	4.93	1.30/1.43	1.48	-	-
Bi ₂ O ₂ Se	4.27/4.27	3.42	4.05/4.05	4.34	1.96/1.96	1.93	-	-
Bi ₂ O ₂ Te	3.60/3.60	3.07	3.76/3.76	5.20	1.71/1.71	1.50	-	-
BiCuOS	2.80/2.80	2.37	3.16/3.16	2.53	1.99/1.99	2.0	2.74/2.74	3.50
BiCuOSe	3.50/3.50	3.00	3.30/3.30	2.81	1.98/1.98	1.93	3.95/3.95	3.26
BiCuOTe	3.47/3.47	2.90	3.05/3.05	2.97	2.26/2.26	2.06	3.56/3.56	2.50

TABLE IV: Projected Grüneisen parameters γ on different atoms and directions in BOX and BiCuOX.

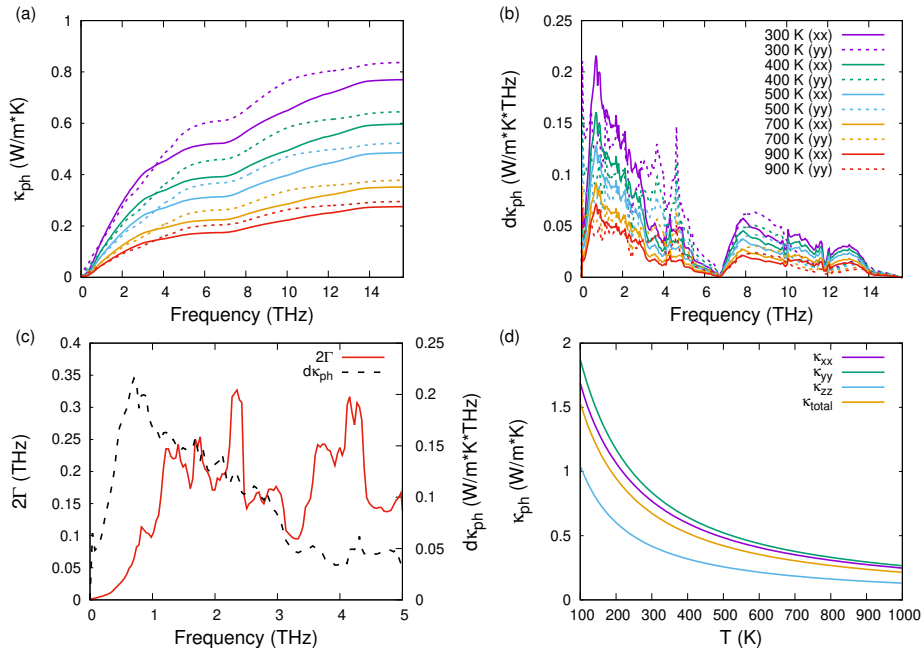


FIG. 7: The phonon transport coefficients of bulk Bi₂O₂S. (a) The accumulative phonon conductivity, (b) Frequency dependence of the in-plane modal phonon conductivity at different temperatures. (c) The frequency dependence of modal phonon conductivity and the phonon line width (2Γ) at room temperature. (d) The phonon thermal conductivity of bulk Bi₂O₂S.

between these two kinds of materials. Figure 11 shows that, κ of BOX and BiCuOX is of similar magnitude. Figure 12 shows that, the phonon band structure contribution to κ is different for these two kinds of materials. BOX would have larger κ than BiCuOX if they have the same relaxation time. Thus, the scattering lifetime τ_λ in BOX is relatively smaller than that in BiCuOX.

There are two possible factors that influence τ_λ . First, Figure 13 shows that, the joint density of states (JDOS) for 3-phonon scattering in BOX are larger than that in BiCuOX.

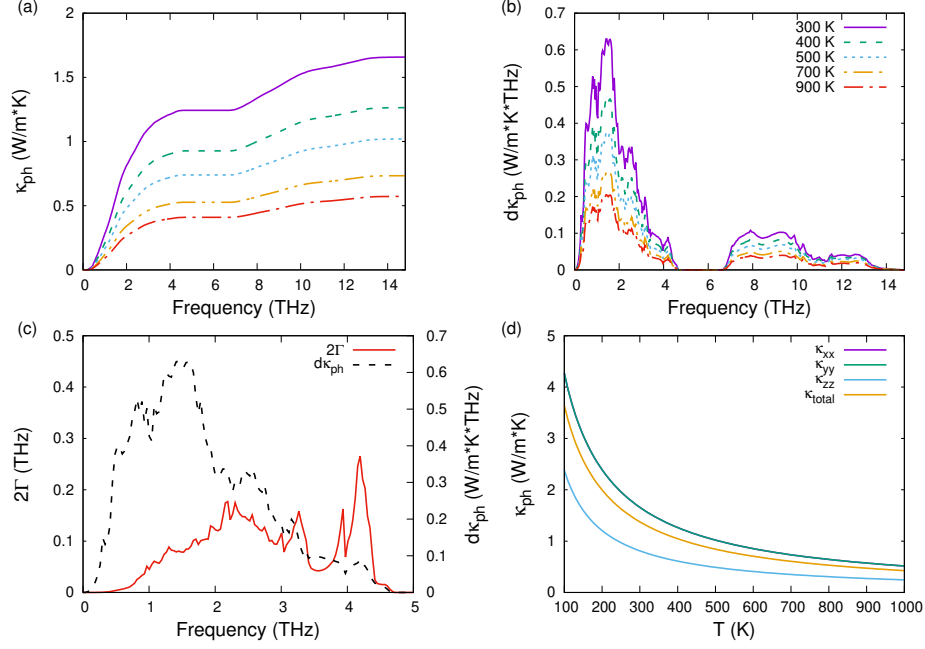


FIG. 8: Similar to Fig. 7 but for $\text{Bi}_2\text{O}_2\text{Se}$.

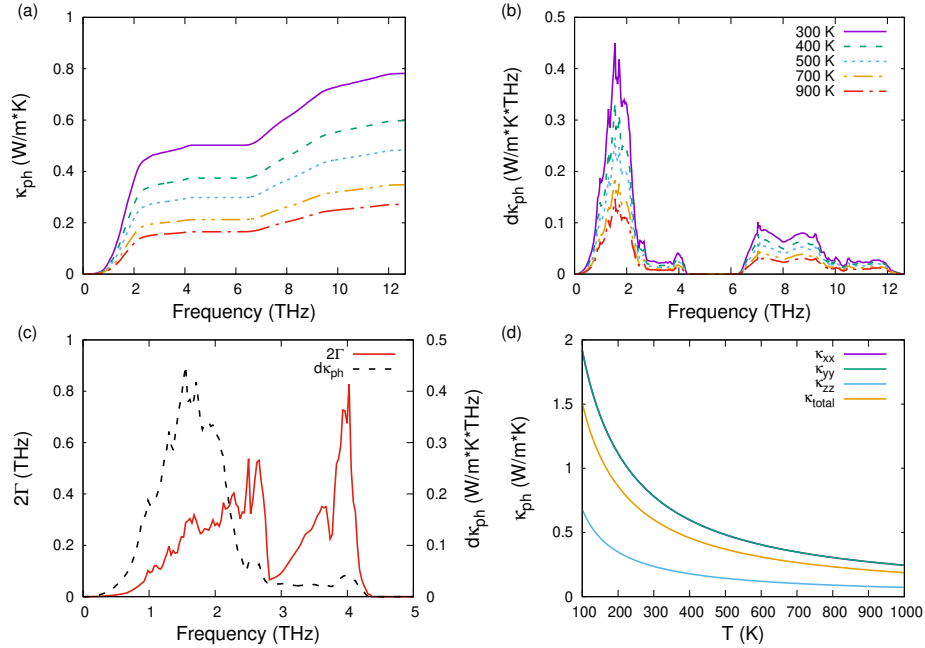


FIG. 9: Similar to Fig. 7 but for $\text{Bi}_2\text{O}_2\text{Te}$.

Larger JDOS gives rise to smaller τ_λ . Second, comparison of projected Grüneisen parameters (Table IV) shows that, the anharmonicity in BOX is larger than that in BiCuOX . Especially, the anharmonicity of inter-layer bonding is stronger in BOX. This can be seen from the relative magnitude of in-plane (x/y) and out-of-plane (z) γ of chalcogen atoms in these two materials. Summing together, both JDOS and the Grüneisen parameters suggest that BOX

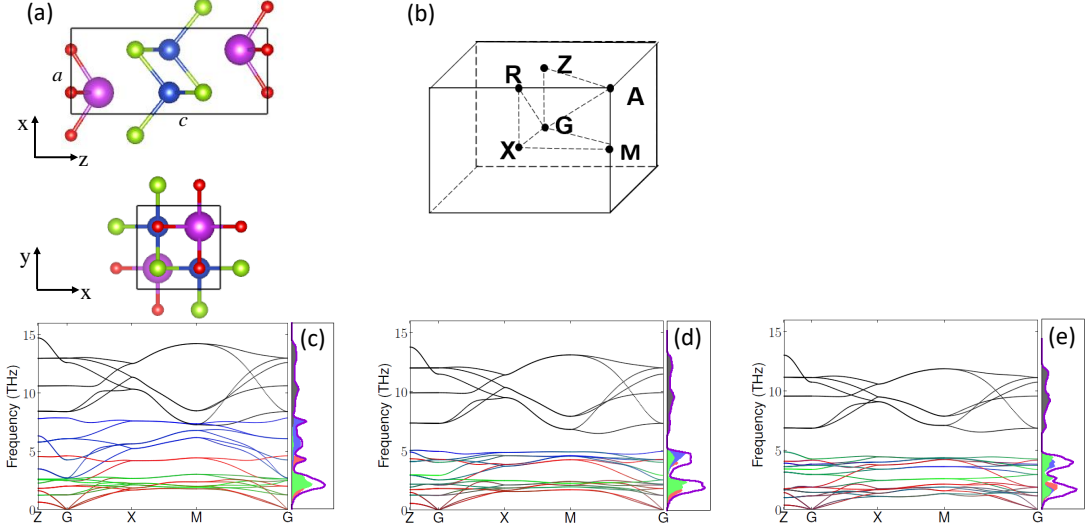


FIG. 10: (a) Side and top view of the atomic structure of BiCuOX (X=S, Se, Te). (b) The high symmetry points in the first Brillouin zone: Γ (0.0, 0.0, 0.0), X (0.5 0.0 0.0), M (0.5, 0.5, 0.0), A (0.5, 0.5, 0.5), R (0.5, 0.0, 0.5), Z (0.0, 0.0, 0.5). (c-e) The atomically-resolved phonon dispersion and density of states. The red, blue, black, green colors correspond to projection onto Bi, chalcogen, O and Cu atoms, respectively.

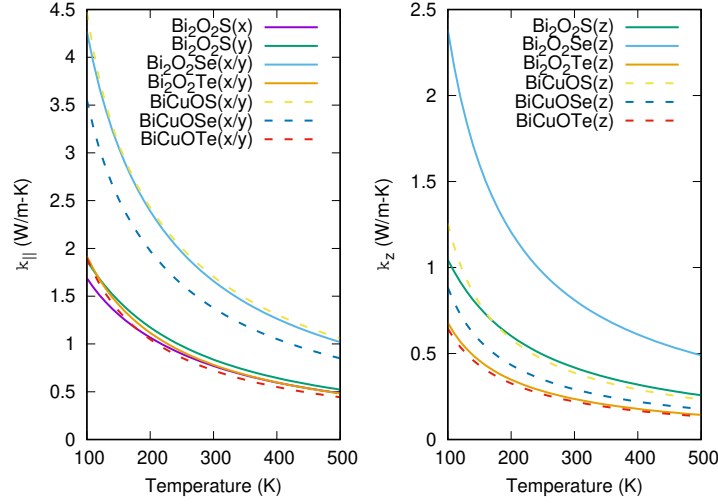


FIG. 11: Comparison of phonon thermal conductivity as a function of temperature between BOX and BiCuOX (X=S, Se, Te). We find the ‘abnormal’ low value of in-plane thermal conductivity for $\text{Bi}_2\text{O}_2\text{S}$.

has a shorter scattering lifetime than BiCuOX. This is actually confirmed in our numerical calculations (Figure 4 in main text and Figure 14).

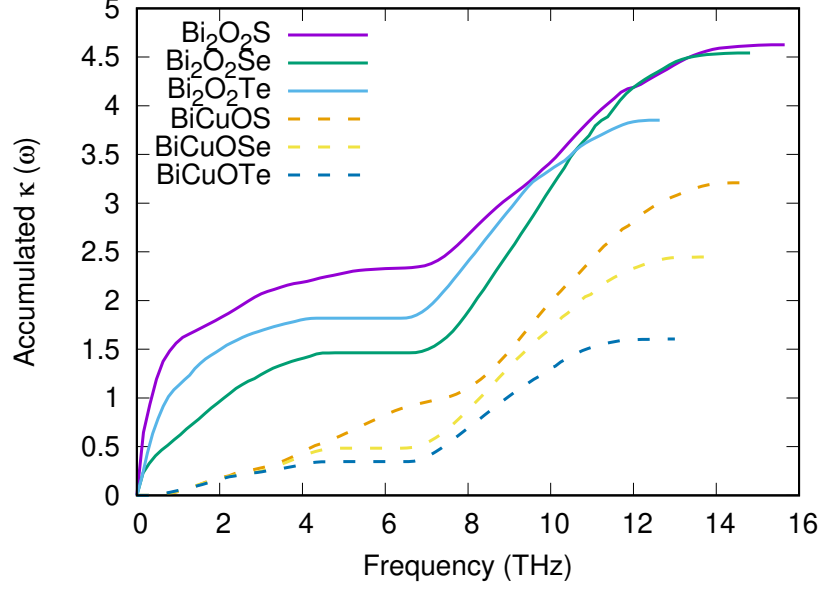


FIG. 12: The relative magnitude of phonon band structure contribution to the accumulated phonon thermal conductivity. It is obtained by setting $\tau_\lambda = 1$ in Eq. (1) of the main text. Comparison between BOX and BiCuOX shows that the former has potential for larger κ when only considering the phonon dispersion.

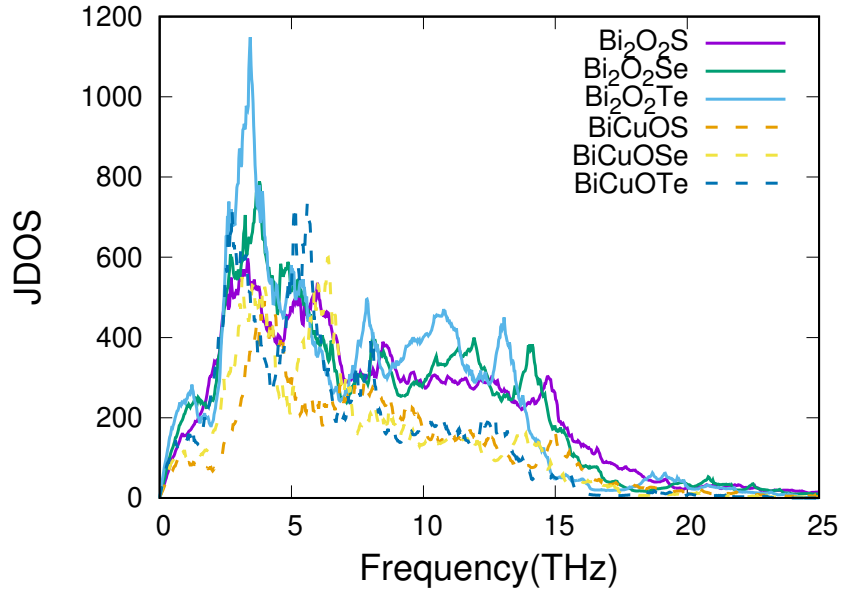


FIG. 13: The JDOS of BOX and BiCuOX. BOX have larger JDOS than BiCuOX, and hence possibly larger scattering rate.

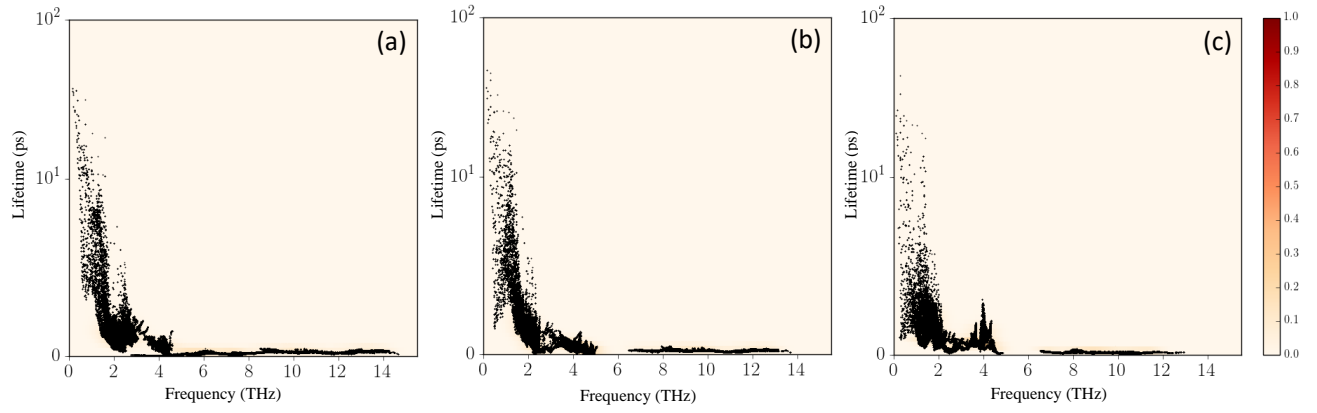


FIG. 14: The distribution of the scattering lifetime as a function of frequency for BiCuOX.

-
- ¹ J. He and T. M. Tritt, *Science* **357**, eaak9997 (2017).
 - ² W. G. Zeier, A. Zevalkink, Z. M. Gibbs, G. Hautier, M. G. Kanatzidis, and G. J. Snyder, *Angew. Chem.* **55**, 6826 (2016).
 - ³ N. Li, J. Ren, L. Wang, G. Zhang, P. Hänggi, and B. Li, *Rev. Mod. Phys.* **84**, 1045 (2012).
 - ⁴ C. Bera, N. Mingo, and S. Volz, *Phys. Rev. Lett.* **104**, 115502 (2010).
 - ⁵ C. J. Vineis, A. Shakouri, A. Majumdar, and M. G. Kanatzidis, *Adv. Mater.* **22**, 3970 (2010).
 - ⁶ M. N. Luckyanova, J. Garg, K. Esfarjani, A. Jandl, M. T. Bulsara, A. J. Schmidt, A. J. Minnich, S. Chen, M. S. Dresselhaus, Z. Ren, E. A. Fitzgerald, and G. Chen, *Science* **338**, 936 (2012).
 - ⁷ W. Li and N. Mingo, *Phys. Rev. B* **91**, 144304 (2015).
 - ⁸ J. Carrete, W. Li, N. Mingo, S. Wang, and S. Curtarolo, *Phys. Rev. X* **4**, 011019 (2014).
 - ⁹ S. Mukhopadhyay, D. S. Parker, B. C. Sales, A. A. Puretzky, M. A. McGuire, and L. Lindsay, *Science* **360**, 1455 (2018).
 - ¹⁰ M. K. Jana and K. Biswas, *ACS Energy Lett.* **3**, 1315 (2018).
 - ¹¹ Y. Zhou and L.-D. Zhao, *Adv. Mater.* **29**, 1702676 (2017).
 - ¹² P. Ruleova, C. Drasar, P. Lostak, C.-P. Li, S. Ballikaya, and C. Uher, *Mater. Chem. Phys.* **119**, 299 (2010).
 - ¹³ S. D. N. Luu and P. Vaqueiro, *J. Solid State Chem.* **226**, 219 (2015).
 - ¹⁴ X. Tan, Y. Liu, K. Hu, G. Ren, Y. Li, R. Liu, Y.-H. Lin, J.-L. Lan, and C.-W. Nan, *J. Am. Ceram. Soc.* **101**, 326 (2018).
 - ¹⁵ S. D. N. Luu and P. Vaqueiro, *J. Materiomics Special Issue on Advances in Thermoelectric Research*, **2**, 131 (2016).
 - ¹⁶ K. Zhang, C. Hu, X. Kang, S. Wang, Y. Xi, and H. Liu, *Mater. Res. Bull.* **48**, 3968 (2013).
 - ¹⁷ J. Wu, H. Yuan, M. Meng, C. Chen, Y. Sun, Z. Chen, W. Dang, C. Tan, Y. Liu, J. Yin, Y. Zhou, S. Huang, H. Q. Xu, Y. Cui, H. Y. Hwang, Z. Liu, Y. Chen, B. Yan, and H. Peng, *Nat. Nanotech.* **12**, 530 (2017).
 - ¹⁸ J. Wu, C. Tan, Z. Tan, Y. Liu, J. Yin, W. Dang, M. Wang, and H. Peng, *Nano Lett.* **17**, 3021 (2017).
 - ¹⁹ J. Yin, Z. Tan, H. Hong, J. Wu, H. Yuan, Y. Liu, C. Chen, C. Tan, F. Yao, T. Li, Y. Chen, Z. Liu, K. Liu, and H. Peng, *Nat. Commun.* **9**, 3311 (2018).

- ²⁰ M. Meng, S. Huang, C. Tan, J. Wu, Y. Jing, H. Peng, and H. Q. Xu, *Nanoscale* **10**, 2704 (2018).
- ²¹ M. Wu and X. C. Zeng, *Nano Lett.* **17**, 6309 (2017).
- ²² C. Chen, M. Wang, J. Wu, H. Fu, H. Yang, Z. Tian, T. Tu, H. Peng, Y. Sun, X. Xu, J. Jiang, N. B. M. Schrter, Y. Li, D. Pei, S. Liu, S. A. Ekahana, H. Yuan, J. Xue, G. Li, J. Jia, Z. Liu, B. Yan, H. Peng, and Y. Chen, *Sci. Adv.* **4**, eaat8355 (2018).
- ²³ J. Wu, C. Qiu, H. Fu, S. Chen, C. Zhang, Z. Dou, C. Tan, T. Tu, T. Li, Y. Zhang, Z. Zhang, L.-M. Peng, P. Gao, B. Yan, and H. Peng, *Nano Lett.* (2018), 10.1021/acs.nanolett.8b03696.
- ²⁴ T. Cheng, C. Tan, S. Zhang, T. Tu, H. Peng, and Z. Liu, *J. Phys. Chem. C* **122**, 19970 (2018).
- ²⁵ A. Togo and I. Tanaka, *Scr. Mater.* **108**, 1 (2015).
- ²⁶ A. Togo, L. Chaput, and I. Tanaka, *Phys. Rev. B* **91**, 094306 (2015).
- ²⁷ J. Carrete, N. Mingo, and S. Curtarolo, *Appl. Phys. Lett.* **105**, 101907 (2014).
- ²⁸ Y. Xiao, C. Chang, Y. Pei, D. Wu, K. Peng, X. Zhou, S. Gong, J. He, Y. Zhang, Z. Zeng, and L.-D. Zhao, *Phys. Rev. B* **94**, 125203 (2016).
- ²⁹ C. W. Li, J. Hong, A. F. May, D. Bansal, S. Chi, T. Hong, G. Ehlers, and O. Delaire, *Nat. Phys.* **11**, 1063 (2015).
- ³⁰ S. Lee, K. Esfarjani, T. Luo, J. Zhou, Z. Tian, and G. Chen, *Nat. Commun.* **5**, 3525 (2014).
- ³¹ H. S. Ji, A. Togo, M. Kaviani, I. Tanaka, and J. H. Shim, *Phys. Rev. B* **94**, 115203 (2016).
- ³² H. Shao, X. Tan, G.-Q. Liu, J. Jiang, and H. Jiang, *Sci. Rep.* **6**, 21035 (2016).
- ³³ A. D. Becke and K. E. Edgecombe, *J. Chem. Phys.* **92**, 5397 (1990).
- ³⁴ G. Kresse and J. Furthmüller, *Phys. Rev. B* **54**, 11169 (1996).
- ³⁵ G. Kresse and J. Furthmüller, *Comp. Mater. Sci.* **6**, 15 (1996).
- ³⁶ J. P. Perdew, K. Burke, and M. Ernzerhof, *Phys. Rev. Lett.* **78**, 1396 (1997).
- ³⁷ H. J. Monkhorst and J. D. Pack, *Phys. Rev. B* **13**, 5188 (1976).
- ³⁸ A. D. Becke and E. R. Johnson, *J. Chem. Phys.* **124**, 221101 (2006).
- ³⁹ F. Tran and P. Blaha, *Phys. Rev. Lett.* **102**, 226401 (2009).